© 2016 IEEE. Personal use of this material is permitted. Permission from IEEE must be obtained for all other uses, in any current or future media, including reprinting/republishing this material for advertising or promotional purposes, creating new collective works, for resale or redistribution to servers or lists, or reuse of any copyrighted component of this work in other works.

Spatial resolution improvement in GNSS-based SAR using multi-static acquisitions and feature extraction

Fabrizio Santi, Marta Bucciarelli, Debora Pastina, Michail Antoniou, Mikhail Cherniakov

***Abstract*—This paper considers the exploitation of navigation satellite systems as opportunity transmitters for bistatic and multistatic SAR. The simultaneous availability of multiple satellites over a scene of interest at different viewing angles allows multi-static SAR acquisitions using a single receiver on or near the ground. The resulting spatial diversity could be used to drastically improve image resolution or to enhance image information space. In order to exploit the availability of multiple satellites, two data fusion approaches are here considered. In the former, point features of the single images obtained from different perspectives are extracted and then combined, whereas in the latter a multistatic image is first obtained by combining the single channel data at the image level and then the point feature are extracted. This is achieved by considering ad-hoc, CLEAN-like techniques. These techniques have been developed on both the analytical and simulation levels, and experimentally verified with real GNSS-based SAR imagery. The techniques described here are not limited to GNSS-based SAR but may be applied to any multi-static SAR system.**

***Index Terms*— passive SAR, GNSS-based SAR, bistatic SAR, multistatic SAR, feature extraction, CLEAN.**

I. Introduction

GLOBAL NAVIGATION SATELLITE SYSTEM (GNSS) signals are available everywhere over the Earth's surface. For such a reason the exploitation of the GNSS for remote sensing have been the focus of an increasing research activity [1]. Many innovative remote sensing applications have been proposed based on the analysis of the GNSS reflected signal (GNSS reflectometry), including, but not limited to, ocean altimetry [2][3], oil spill detection [4], soil moisture and biomass estimation [5], wind speed and direction estimation [6]. Since navigation satellites operate in the microwave region, such signals have been also considered as opportunity transmitters for Passive Coherent Location (PCL) systems [7]-[9].

One of the emerging technologies based on GNSS transmissions is in the field of the Bistatic Synthetic Aperture Radar (BSAR) [10]. This topic has been investigated for a number of years on both the theoretical and experimental levels, and its feasibility for imaging as well as potential for area monitoring has been experimentally verified [10]-[16]. An airborne/ground moving or stationary receiver can collect the signal emitted from a GNSS satellite, such as the Global Positioning System (GPS), GLObal NAvigation Satellite System (GLONASS), or the forthcoming Galileo and Beidou, and reflected from an area of interest [10]. In the case of a moving receiver, the aperture is synthesized by exploiting the motion of the platform carrying the receiver itself, whereas in the case of a stationary receiver, the motion of the satellite produces the Doppler gradient making possible the azimuth resolution. This paper considers a fixed, ground based receiver configuration, but without loss of generality, the algorithms proposed can be used in any of the topologies mentioned above.

From a radar perspective, there are a number of benefits deriving from the choice of navigation satellites as transmitters. Their global coverage ensures that any point of the Earth's surface is constantly illuminated by GNSS signals, offering the potential for persistent area monitoring, for example using change detection techniques [14][15][17]. In addition, the multitude of satellites above any point on Earth enables multi-static SAR acquisitions, that may be used to enhance image information space or fused together to enhance image properties. Moreover, GNSS transmit in L-band, suitable for Earth observation. From a technology point of view the system is cost effective, since only the receiver needs to be designed and developed, and its hardware is very similar, if not identical, to standard navigation receiver chipsets. On the other hand, GNSS signals are not designed for radar applications, entailing several issues to be faced. One of the main problem is represented by the power budget, since the power density near the Earth's surface is very low. However, sufficiently high Signal-to-Noise Ratios (SNR) may be achieved by long dwell time on target, which is in the order of several minutes for a fixed receiver. The major system bottleneck is the achievable performance in terms of spatial resolution. The azimuth resolution may be sufficiently high if long dwell times are used (3-4m for 4-5mins dwell), however range resolution is restricted

Manuscript received September 4, 2015; revised March 17, 2016; accepted May 14, 2016. Date of publication XXX; date of current version XXX.

F. Santi, M. Bucciarelli and D. Pastina are with the Dipartimento di Ingegneria dell'Informazione, Elettronica e Telecomunicazioni (DIET), Sapienza University of Rome, 00184 Rome, Italy (e-mail: santi@diet.uniroma1.it).

M. Antoniou and M. Cherniakov are with the School of Electronic, Electrical and Computer Engineering, University of Birmingham, Birmingham B15 2TT, U.K. (e-mail: m.antoniou@bham.ac.uk).

Color version of one or more of the figures in this paper are available online at http://ieeexlporer.ieee.org.

Digital Object Identifier XXXXX.

to the ranging signal bandwidth. For example, the Galileo E5bQ signal has a bandwidth of about 10 MHz, offering a resolution of 15 m in the quasi-monostatic case (and 30m for the GLONASS P-code) and is further degraded in bistatic geometries. This limitation restricts the field of applications for this technology. For this reason, a number of different methods to increase image resolution have been investigated. In [18], it was found that very long dwell times tend to increase range, as well as azimuth resolution due to the curvature of the satellite trajectory, but to gain an essential increase the dwell times on target has to substantially increase to tens of mins. Considering Galileo only, it was shown that it is possible to join its E5 sub-bands to increase range resolution to 3m in theory, but this technique is limited to Galileo and introduces essential reduction in SNR [19].

Now, the possibility to increase image resolution by considering multi-static GNSS-based SAR acquisitions is being investigated. The motivation is that at any time of the day and at any point of the Earth's surface, 4-8 GNSS satellites are simultaneously visible over the horizon for a single constellation, and potentially this number can be increased up to 24-32 when all the navigation satellites systems are fully operational. Working with point-like targets, it has already been experimentally shown that a non-coherent combination of GNSS-based SAR images obtained by spatially separated satellites may drastically improve image resolution [20]. As a consequence of the enhanced resolution, the amount of information of the observed area may be increased, that may help in extracting the feature of the scene for its characterization; however for complex imaging scenes these methods introduce artefacts to be corrected [21].

As well as the possibility of combining the single BSAR in a multistatic SAR (MSAR) image, the large amount of satellites illuminating the area from different view angles may be used to enhance image information space. To the purpose, some specific features characterizing the scene are extracted from each image and subsequently combined. Such a combination strategy at the feature level, here referred to as multi-perspective imaging, can provide significant increase in target information, leading to enhanced classification performance [22]. In the framework of GNSS-based SAR images, a multi-perspective analysis has been considered for terrain classification purposes exploiting GLONASS satellites in [23], based on the variation of the radar cross section (RCS) of different targets at various bistatic geometries; recently, an experimental study using the Chinese navigation system BeiDou-2 has been carried out, based on a region-of-interest segmentation approach [24].

Both the multi-perspective and multistatic imaging approaches have been proved able to provide a better understating of the interrogated area, and the choice of a specific strategy essentially depends on the particular feature employed to characterize the scene, such as point [25], linear [26] or textural [27] features. In this work, we aim at identifying the dominant scattering centers of the scene. To this purpose, CLEAN algorithms are considered. The main idea of the CLEAN is successively identifying and removing the brightest target in the image by subtracting the point spread function (PSF) of the system centered at the location of the selected spot and scaled accordingly to its intensity so that even weak targets become progressively visible, [28]; over the last years several CLEAN-like algorithms have been proposed in SAR literature [29][30]. Here, ad-hoc CLEAN techniques able to deal with the GNSS-based SAR images are considered. First, by applying a proper bistatic CLEAN algorithm to the individual images, the scattering centers can be extracted and then the information arising from the different single channels can be combined. Moreover, a multistatic CLEAN algorithm is proposed able to deal with the MSAR image. Since a GNSS-based multistatic SAR image may be characterized by a drastically improved PSF (with respect to the bistatic image), more information can be extracted in this case and details of the image can be identified; in addition, it will be shown the capability of this algorithm to correct the artefacts arising in the multistatic acquisition. Very preliminary results concerning this topic have been presented in [31]. In order to foresee the predictable performance of these feature extraction approaches on real images, a performance analysis against emulated images composed by experimental point-like targets has been carried on. The developed techniques have been then applied against experimental bi/multi-static images. The combination of the single point features extracted from different BSAR images shows how the multi-perspective imaging is a feasible approach in the context of GNSS-based SAR to increase the knowledge about the structure of the observed area. Moreover, the extraction of the features from the MSAR image can strongly enhance the quality of the image information, as a consequence of the image resolution improvement and the artefacts correction, thus allowing the identification of details of the area.

The remainder of the paper is organized as follows: the GNSS-based SAR system is described in Section II; in Section III, the developed CLEAN techniques for the feature extraction from the BSAR and MSAR images are presented and their performance are analyzed in Section IV; in Section V we show the results achieved against real images and Section VI concludes the paper.

II. GNSS-BASED SAR

The GNSS-based SAR topology is sketched in Fig. 1, where the positions of transmitters, receiver and targets are described in the East-North-Up (ENU) reference system. The operative condition is given by a ground-based stationary receiver collecting the signals emitted from N GNSS transmitters and reflected by a stationary scene. The receiver is able to separate the signals coming from different satellites by using frequency or coding division approaches. By properly processing the data [11], [32], from each bistatic link a different BSAR image is obtained.

Due to the very coarse resolution resulting from this passive SAR system, the scene can be considered as composed by a set of isolated and point-like targets, and more complicated scattering phenomena valid for high-resolution images can be neglected. Therefore, the interrogated area can be considered as a map of K independent scattering centers and the ith BSAR

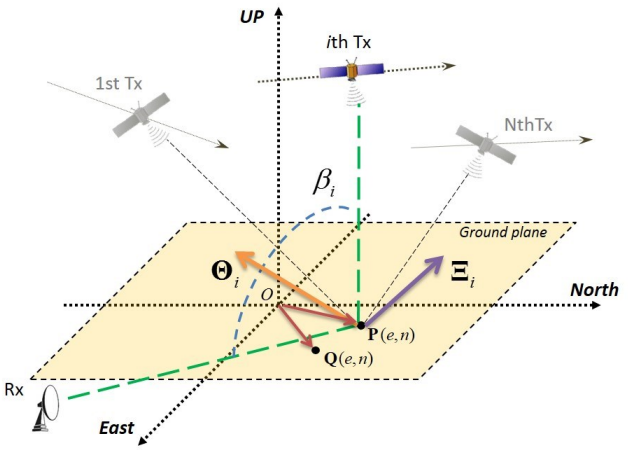

Fig. 1. GNSS-based SAR topology.

image I_i can be approximated as the superposition of the PSF of each scatterer centered on its position (e_k, n_k) and properly scaled according to a complex coefficient accounting for its reflectivity.

$$I_i = \sum_{k=1}^{K} \xi_{i,k} \chi_i(e - e_k, n - n_k) \quad (1)$$

where e represents the East-axis and n the North-axis, $\xi_{i,k}$ is the complex reflectivity of the kth scatterer (modulus $A_{i,k}$) and finally $\chi_i(e,n)$ is the system PSF.

The PSF of the system can be described by means of the Generalized Ambiguity Function (GAF) [33]; let **P** be the vector position of a desired point reflector to be evaluated and vector **Q** an arbitrary position of another reflector in the vicinity of **P**, the GAF is given by

$$\chi_i(\boldsymbol{P},\boldsymbol{Q}) = p\left(\frac{2\cos\left(\beta_i/2\right)\boldsymbol{\Theta}_i^T(\boldsymbol{Q}-\boldsymbol{P})}{c}\right) \times m\left(\frac{2\omega_{E_i}\boldsymbol{\Xi}_i^T(\boldsymbol{Q}-\boldsymbol{P})}{\lambda}\right) \times \exp\{j\varphi_i(\boldsymbol{Q},\boldsymbol{P})\} \quad (2)$$

where $p(\cdot)$ is the matched filter output of the ranging signal and it specifies the range resolution properties, being β_i the bistatic angle relative to scatterer **P** (i.e. the angle between the line-of-sights connecting the ith transmitter and receiver to the scatterer **P**) and $\boldsymbol{\Theta}_i$ the unit vector lying on its bisector and defining the range resolution direction. $m(\cdot)$ is the inverse Fourier transform of the normalized signal magnitude pattern and specifies the Doppler characteristics of the system; it depends on the equivalent angular speed ω_{E_i} and the unit vector $\boldsymbol{\Xi}_i$, referred to as the equivalent motion direction, that defines the Doppler resolution direction for scatterer **P**. c is the speed of light and λ the wavelength. φ_i is the phase term accounting for the point reflector position, given by $\frac{2\pi}{\lambda}\left(2\cos\left(\beta_i/2\right)\boldsymbol{\Theta}_i^T(\boldsymbol{Q}-\boldsymbol{P})\right)$. T is the transpose operator. It has to be underlined that in (2) all the geometry related parameters (the bistatic angle β_i, the unit vector $\boldsymbol{\Theta}_i$, the equivalent angular speed ω_{E_i} and the unit vector $\boldsymbol{\Xi}_i$) are specifically referred to and defined with respect to the scatterer with position vector **P** (see [33] for all the detailed definitions). This implies that the system PSF is essentially spatially variant, namely it slightly changes its characteristics as the position **P** changes over the imaged area. However, it is expected and verified through simulated and experimental data that those differences diminish as the distance between the considered scatterer and the receiver position increases.

A slice of $|\chi_i(\boldsymbol{P},\boldsymbol{Q})|$ onto the ground plane is approximately an ellipse, referred to as resolution ellipse, characterized by its orientation ϕ_i, depending on the satellite position and trajectory. Therefore, when transmission from multiple satellites is considered, a set of BSAR images characterized by PSFs with essentially different orientations are obtained.

Due to the limited transmitted bandwidth, the bistatic geometry and the consequent non-orthogonality between range and Doppler resolution directions [34], each I_i is characterized by a coarse spatial resolution (generally resolution cell area in the order of 80-150 m^2), whose worst value coincides with the direction of the resolution ellipse. As an example, we consider a simulated scenario given by a ground-based receiver collecting the signals reflected by a point scatterer in the scene center illuminated by the P-codes transmitted by two GLONASS satellites (5.11 MHz bandwidth). The parameters of the simulation are reported in Table I. In this example, the satellites have been chosen in a way that their bistatic PSF orientations are nearly orthogonal for illustration. The corresponding images, shown in Fig. 2a and b in the intensity domain (log-scale), represent the PSFs (or image responses) of the system. As it is apparent, wide resolution cell areas have been obtained for both the cases, with area (hereinafter evaluated at the -3 dB cut) equal to 98 m^2 and 95 m^2, respectively.

Nevertheless, considering the different orientation of the bistatic PSFs, as well as the possibility of obtaining multiple views of the same area, the GNSS-based SAR makes possible to form a multistatic image that can be drastically improved in terms of spatial resolution with respect to the single bistatic images: the individual images obtained by multiple, spatially separated satellites can be combined thus forming a MSAR image whose resolution cell area is the overlapping segment of the single bistatic PSFs, and therefore may be essentially reduced. To this purpose, both coherent and non-coherent

TABLE I
SIMULATED ACQUISITIONS PARAMETERS

i	Satellite (Cosmos)	β_i [deg]	ω_{E_i} [deg/sec]	Dwell time [sec]
1	716	100.14	0.0050	300
2	717	85.54	0.0049	250

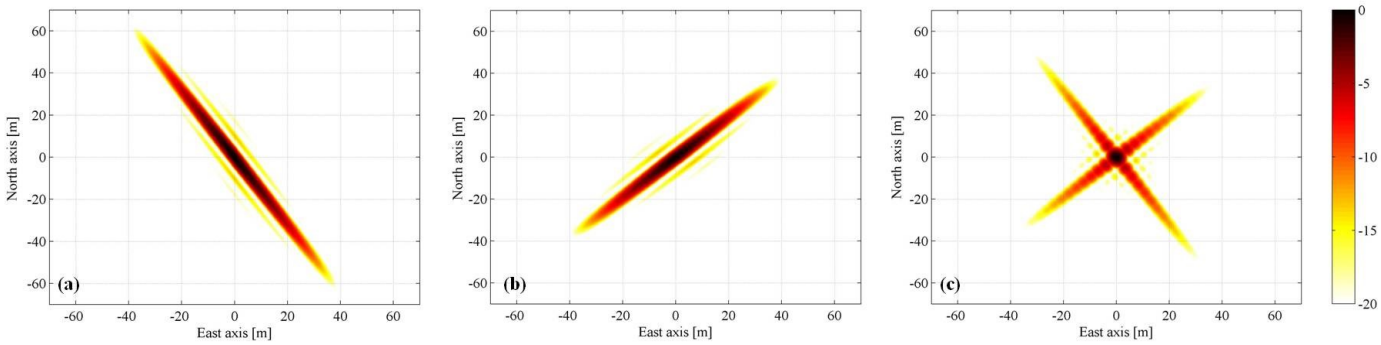

Fig. 2. Bistatic and multistatic PSFs – a) bistatic PSF $i = 1$, b) bistatic PSF $i = 2$, c) multistatic PSF.

methods could be applied. However, we have to consider that the complex amplitude of a real scatterer is fluctuating between observations from different view angles, and amplitude and phase terms of the target reflectivity are a priori unknown. In such conditions, to guarantee the scatterer coherence when imaged at multiple bistatic geometries is a very challenging issue. For this reason, in this work the non-coherent combination method has been considered. The multistatic PSF of such a system is achieved by non-coherently adding the N responses of a point scatterer as imaged in the set of bistatic images [20]

$$\bar{\chi}(\boldsymbol{P},\boldsymbol{Q}) = \frac{1}{N}\sum_{i=1}^{N}\left| p\left(\frac{2\cos\left(\beta_i/2\right)\boldsymbol{\theta}_i^T(\boldsymbol{P},\boldsymbol{Q})}{c}\right) \times m\left(\frac{2\omega_{E_i}\boldsymbol{\Xi}_i^T(\boldsymbol{P},\boldsymbol{Q})}{\lambda}\right)\right| \quad (3)$$

Fig. 2c shows the image response obtained by combining the single channel images, which area is 20 m^2. Therefore, an improvement factor in spatial resolution of about 5 has been obtained with respect to the bistatic images.

When we move from the point target analysis to real scenarios, we have to take into account that the bistatic RCS of a target is essentially different from the monostatic case [35], and different bistatic geometries result in target RCS variation; as anticipated, a fair model of the scene has to take into account an anisotropic behavior for the multistatic response of the kth scatterer (i.e., generally $\xi_{i,k} \neq \xi_{h,k}$ for $i \neq h$). Therefore, the contribution to the multistatic image of a single scatterer can be written as the linear combination of the absolute values of the responses $|\chi_i(e - e_k, n - n_k)|$ with the amplitude coefficients $A_{i,k}$, and the resulting MSAR image is given by

$$I_M = \frac{1}{N}\sum_{i=1}^{N}|I_i| = \frac{1}{N}\sum_{i=1}^{N}\sum_{k=1}^{K} A_{i,k}|\chi_i(e - e_k, n - n_k)| \quad (4)$$

It stands to reason that, despite the different amplitude coefficients due to the anisotropic behavior of the scatterer, a considerable improvement in the resolution capability with respect to the bistatic case can be achieved. For example, if the amplitude of the scatterer in Fig. 2b is half the one in Fig. 2a, the area of the multistatic return is 22 m^2, thus moving from an improvement factor in spatial resolution with respect to the bistatic cases of about 5 in the optimum case (same scatterers amplitude in different images) to 4.5.

Despite the potential of the non-coherent combination of the BSAR images to improve the spatial resolution of the system, some fundamental issues arise. As will be shown later on, the main issue is that the non-coherent combination of multiple coarse resolution images introduces regions of apparent high echo intensity in a multi-static image, which falsely appear as target returns, i.e. ghost targets [21]. We will show in the remainder of the paper how the developed feature extraction technique for the multistatic scenario gets the capability to reject such artefacts.

III. CLEAN Techniques for GNSS-Based SAR

The features of the GNSS-based bi/multi-static SAR images can be extracted in terms of amplitude and position of the dominant scattering centers. To the purpose, ad-hoc CLEAN techniques are here described. Both the bistatic and multistatic scenarios have been considered, based on the image models in (1) and (4), respectively. In the former, a GNSS-based BSAR coherent CLEAN technique has been developed; by applying the bistatic CLEAN to the set of N BSAR images, the single channel information can be extracted and then combined, thus allowing a multi-perspective analysis of the area. In the latter, a joint bistatic/multistatic CLEAN technique is proposed able to work with a MSAR image, and therefore suitable for the multistatic image analysis.

A. CLEAN for BSAR images

The bistatic CLEAN algorithm, as depicted in Fig. 3, is an iterative procedure whose kth iteration consists of the following four steps:

1. The dominant scatterer in the BSAR image I_{test} is selected as the scatterer corresponding to the maximum intensity response in the image. A region is inhibited around the position of a previously extracted scatterer to avoid that the algorithm uselessly loops due to artefacts arising from the image update procedure. At the first iteration the image I_{test} corresponds to the original BSAR image. Indeed due to the limited accuracy of the estimations of the actual amplitude and position of the previously extracted scattering centre, there could be a misalignment between the real scattering response in the currect image and the theoretical PSF properly scaled and

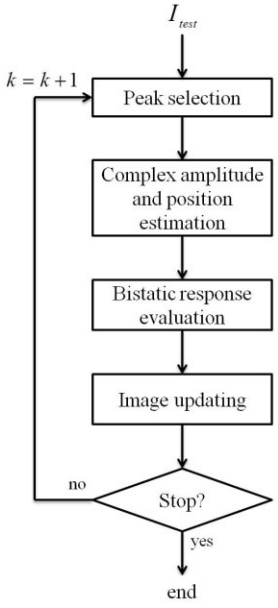

Fig. 3. Coherent CLEAN for bistatic images processing scheme.

positioned according to the estimated parameters. Since the update procedure is accomplished by means of a coherent subtraction, as it will be clearly explained in the following, this could generate artefacts mainly on the edges of the PSF main lobe that could be unfortunately recognized as dominant scatterers in the subsequent iterations of the CLEAN procedure. To this purpose an inhibited region is defined and achieved applying a null mask centered in the position of the previous extracted scatterer, whose shape follows the shape of a properly saturated and normalized theoretical system PSF. Obviously the level of the saturation defines the extension of the region to be inhibited.

2. When the dominant scatterer has been identified, the goal of the CLEAN algorithm is to subtract its contribution from the image after a proper estimation stage. Two possible strategies for cancelling the scatterer can be employed: non-coherent subtraction and coherent subtraction. The non-coherent cancellation stage is expected to induce strong changes in the area near the extracted scatterer where the subtraction takes place, thus worsening the estimation of the unknown parameters for close scatterers. Therefore the non-coherent processing scheme for CLEAN seems to be suitable when the interest is in extracting geometric features rather than radiometric. On the other hand, a coherent implementation is expected to preserve the information of the area near the scatterer after its cancellation, allowing a better identification of the remainder scatterers in the neighborhood and providing more accurate amplitude estimations. Therefore for the present analysis a vector of unknowns for the generic kth scatterer is defined as

$$\boldsymbol{Y}_k = [A_{kR}, A_{kI}, e_k, n_k] \tag{5}$$

where A_{kR} and A_{kI} are the real and imaginary parts of the scatterer reflectivity ξ_k, respectively, i.e. $\xi_k = A_{kR} + jA_{kI}$. Unknowns are estimated in the least square sense by minimizing the energy of the error. First of all a patch I_{sel} of the image containing the kth dominant scatterer is identified: the patch is achieved nulling all the image except for a region around the extracted kth dominant scatterer shaped as a properly saturated normalized theoretical PSF. Obviously the level of the saturation defines the extension of the patch to be considered. The error is computed as the coherent difference between the patch of the image containing the selected scatterer I_{sel} and the model of the BSAR response $\mathrm{S}(\mathbf{Y}_k)$. The initial values for the minimization are set to be equal to the position of the peak in the image and to the complex amplitude of the pixel associated to the dominant scatterer extracted in the first step

$$\min_{\mathbf{Y}_k} \text{sum}\{|\mathrm{S}(\mathbf{Y}_k) - I_{sel}|^2\} \tag{6}$$

S is a function of the parameters to be estimated contained in the vector $\mathbf{Y}_k$. In particular, the response model is

$$\mathrm{S}(\mathbf{Y}_k) = \xi_k \chi(e - e_k, n - n_k) \tag{7}$$

3. The estimated response for the kth scattering centre extracted from the image is computed as a function of the estimated parameters $\widehat{\mathbf{Y}}_k$

$$\hat{\mathrm{S}}_k = \mathrm{S}(\widehat{\mathbf{Y}}_k) \tag{8}$$

4. The image I_{test} is updated for the following iteration

$$I_{test} = \left(I_{test} - \hat{\mathrm{S}}_k\right) \tag{9}$$

Steps from 1 to 4 are repeated: at the end, the matrix $\widehat{\mathbf{Y}}$ contains a number of rows $\widehat{\mathbf{Y}}_k$ equal to the number of extracted scattering centers. The algorithm ends when a stop condition is reached: in our case this condition is fulfilled when the energy of the residual image is below a certain threshold that can be a percentage of the energy of the starting image or when all the remaining valid peaks are under a certain dynamic.

B. Joint bistatic/multistatic CLEAN for MSAR images

Unlike the BSAR images, the phase information is not retained in the MSAR image, (4). Therefore, the CLEAN technique as described in the previous section cannot be directly applied in the multistatic scenario. A possibility could be to give up the estimation of the complex return from the scatterer, and perform a non-coherent updating of the image. Nevertheless, we already discussed how the full complex reflectivity estimation can result in improved performance. However, the phase information is still preserved in the single BSAR images. In order to perform a coherent updating of the MSAR image, a joint bistatic/multistatic CLEAN for MSAR images is here proposed. It comprises the four steps described in the following (see Fig. 4):

1. The dominant scatterer in the MSAR image I_{test} is

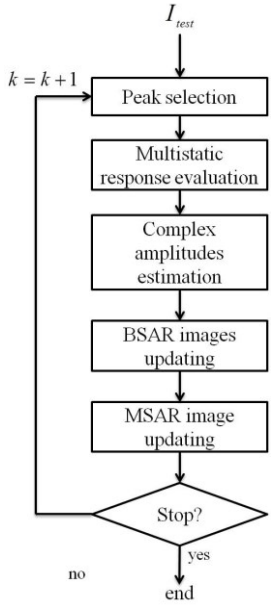

Fig. 4. Joint bi/multi-static CLEAN for multistatic images processing scheme.

selected as the scatterer corresponsing to the maximum intensity response in the image. At the first iteration the image I_{test} corresponds to the original MSAR image. Moreover, the ith bistatic image I_{test-i} is initialized as the original ith BSAR image, for $i = 1, \dots, N$.

2. The unknown vector is defined as

$$\mathbf{Y}_{\mathrm{k}} = [\mathrm{A}_{1\mathrm{kR}}, \mathrm{A}_{1\mathrm{kI}} \ \dots, \ \mathrm{A}_{\mathrm{NkR}}, \ \mathrm{A}_{\mathrm{NkI}}, \mathrm{e}_{\mathrm{k}}, \mathrm{n}_{\mathrm{k}}] \qquad (10)$$

and its elements are estimated in two steps by exploiting both BSAR and MSAR images as in the following. First step aims at estimating the scatterer position and at providing a first raw estimate for the scatterer reflectivity which is then refined in the second step.

a. The modulus of the amplitude coefficients for the kth scatterer and its position $\mathbf{Y}_{\mathrm{Mk}} = [A_{1k}, \dots, A_{Nk}, \mathrm{e}_{\mathrm{k}}, \mathrm{n}_{\mathrm{k}}]$ are estimated from the MSAR image using a non-coherent multistatic version of CLEAN as in section IIIA. It has to be underlined that for the same scatterer the real reflectivity coefficients A_{ik} are considered as different in different bistatic images. The response model can be written as

$$S(\mathbf{Y}_{\mathrm{Mk}}) = \sum_{i=1}^{N} \mathrm{A}_{ik} |\chi_i(e - e_k, n - n_k)| \qquad (11)$$

and the update step is performed as in (9) being the image I_{test} equal to the multistatic image I_M at first iteration and the vector $\hat{\boldsymbol{Y}}_{Mk}$ the estimation of the unknowns in (10). Thanks to the enhanced resolution of the multistatic image with respect to the bistatic ones, the position $(\hat{\mathrm{e}}_{\mathrm{k}}, \hat{\mathrm{n}}_{\mathrm{k}})$ of the scatterer estimated at this stage is assumed as the final estimations, whereas the N amplitudes are used as initial values for the following stage.

b. The real and imaginary parts of the N complex amplitudes $(\mathrm{A}_{1\mathrm{kR}}, \mathrm{A}_{1\mathrm{kI}} \ \dots, \ \mathrm{A}_{\mathrm{NkR}}, \ \mathrm{A}_{\mathrm{NkI}})$ are estimated by minimizing a joint BSAR-MSAR error function. The patches I_{sel-i} $(i = 1, \dots, N)$ and I_{sel} containing the identified scatterer are extracted from the ith bistatic image and the multistatic image respectively. For the BSAR patches an error function is computed as the coherent difference between the patch and the model of the BSAR response $\mathrm{S}_i(\mathbf{Z}_{ik}, \hat{e}_k, \hat{n}_k)$ where $\mathbf{Z}_{ik} = [\mathrm{A}_{ik\mathrm{R}}, \mathrm{A}_{ik\mathrm{I}}]$, while for the MSAR patch a non-coherent difference with the multistatic response $\mathrm{S}(\mathbf{Z}_{Mk}, \hat{e}_k, \hat{n}_k)$ is taken into account where $\mathbf{Z}_{Mk} = [A_{1k}, \dots, A_{Nk}]$. $\mathrm{S}_i(\mathbf{Z}_{ik}, \hat{\mathrm{e}}_{\mathrm{k}}, \hat{\mathrm{n}}_{\mathrm{k}})$ is computed as in (7), while $\mathrm{S}(\mathbf{Z}_{Mk}, \hat{\mathrm{e}}_{\mathrm{k}}, \hat{\mathrm{n}}_{\mathrm{k}})$ is defined as in (11). The considered cost function used for the estimation of the complex amplitude coefficient is a linear combination of the single bistatic/multistatic cost functions

$$\min_{(\mathbf{Z}_{1k} \ \dots, \mathbf{Z}_{Nk})} \begin{Bmatrix} \mathrm{sum}\,[|\mathrm{S}_1(\mathbf{Z}_{1k}, \hat{\mathrm{e}}_{\mathrm{k}}, \hat{\mathrm{n}}_{\mathrm{k}}) - I_{sel-1}|^2] + \\ + \cdots + \\ + \mathrm{sum}\,[|\mathrm{S}_N(\mathbf{Z}_{Nk}, \hat{\mathrm{e}}_{\mathrm{k}}, \hat{\mathrm{n}}_{\mathrm{k}}) - I_{sel-N}|^2] \\ + \mathrm{sum}\,[|\mathrm{S}(\mathbf{Z}_{Mk}, \hat{\mathrm{e}}_{\mathrm{k}}, \hat{\mathrm{n}}_{\mathrm{k}}) - I_{sel}|^2] \end{Bmatrix} \qquad (12)$$

Uniform weights are used in the combination of the cost functions in order not to favor bistatic or multistatic images. Moreover, the obvious equality $\mathrm{A}_{ik} = \sqrt{A_{ikR}^2 + A_{ikI}^2}$ holds.

3. At the end of the estimation procedure, N complex bistatic reponses from the kth scatterer are obtained as a function of the estimated parameters and collected in the vector $\hat{\mathbf{Z}}_{ik} = [\hat{A}_{ikR}, \hat{A}_{ikI}]$ for $i = 1, \dots, N$

$$\hat{\mathrm{S}}_{ik} = \mathrm{S}_i(\hat{\mathbf{Z}}_{ik}, \hat{\mathrm{e}}_{\mathrm{k}}, \hat{\mathrm{n}}_{\mathrm{k}}) \qquad (13)$$

4. The multistatic image I_{test} is updated for the successive iteration

$$I_{test} = \sum_{i=1}^{N} |I_{test-i} - \hat{\mathrm{S}}_{ik}| \qquad (14)$$

Eq. (14) also defines the corresponding update on the different BSAR images. Steps from 1 to 4 are repeated: at the end, the matrix $\hat{\mathbf{Y}}$ contains a number of rows $\hat{\mathbf{Y}}_k = [\hat{\mathbf{Z}}_{1k} \ \dots, \hat{\mathbf{Z}}_{Nk}, \hat{\mathrm{e}}_{\mathrm{k}}, \hat{\mathrm{n}}_{\mathrm{k}}]$ equal to the number of extracted scattering centers. The algorithm ends when a stop condition is reached: as previously stated this condition is fulfilled when the energy of the residual image is below a certain threshold that can be a percentage of the energy of the starting image or when all the remaining valid peaks are under a certain dynamic.

IV. Performance Analysis

The performance of the developed GNSS-based CLEAN

TABLE II
ACQUISITIONS PARAMETERS OF EXPERIMENTAL BISTATIC PSFS

#	Satellite (Cosmos)	β [deg]	ω_E [deg/s]	Dwell time [s]
1	736	102	0.0047	300
2	732	74	0.0048	300

techniques are here analyzed against images composed by close point targets. In order to analyze the performance in a realistic scenario, experimental PSFs are employed in order to emulate real images. The experimental bistatic PSFs have been obtained by using the direct signal from the satellite collected by a low-gain antenna, acting itself like a point-scatterer [18]-[20]. Signals emitted by two GLONASS satellites have been collected, and the parameters of the acquisitions are reported in Table II.

In order to analyze the capability of the bistatic CLEAN at extracting close scattering centers, the following emulated scenario has been considered: a BSAR image composed by $K = 2$ close point scatterers located in $\boldsymbol{P}_1 = (\mathrm{e}_1, \mathrm{n}_1)$ and $\boldsymbol{P}_2 = (\mathrm{e}_2, \mathrm{n}_2)$ has been emulated by coherently adding experimental PSFs concerning geometry #1 with a phase difference $\Delta\varphi$; such phase difference is selected accordingly to a uniform distribution in $(-\pi, \pi]$ and a white Gaussian noise has been added to the image, such that the peak SNR is equal to 25 dB; the bistatic CLEAN is applied and the position and amplitude of the revealed scattering centers are estimated as $\widehat{\boldsymbol{P}}_k$ and $\hat{A}_k$; if the greatest error of the estimated positions $\delta p_k = |\widehat{\boldsymbol{P}}_k - \boldsymbol{P}_k|$ is smaller than Δp and the error of the estimated scatterer's amplitude $\delta A_k = |\hat{A}_k - A_k|$ is at worst ΔA, we consider that the algorithm has correctly extracted the feature of the scene. Such an analysis has been carried out for 100 independent trials for each point of a grid $(\Delta\mathrm{e}, \Delta\mathrm{n})$, being the offsets in the location of the second scatterer with respect to $\boldsymbol{P}_1$, i.e. $(\Delta\mathrm{e}, \Delta\mathrm{n}) = \boldsymbol{P}_2 - \boldsymbol{P}_1$. The obtained results in terms of probability of correctly extracted features $P_{c.e.}$ are shown in Fig. 5. As stated in Section II, the worst spatial resolution direction of the BSAR is represented by the direction of the major axis of the resolution ellipse, ϕ. Therefore, if the two scattering centers are aligned along such a direction, a worsening of the CLEAN performance with respect to other directions is expected. Indeed, in Fig. 5 we can observe a notch of $P_{c.e.}$ around the red solid line, representing the direction of the major axis of the resolution ellipse concerning the scatterer in $\boldsymbol{P}_1$. Therefore, in the bistatic case a considerable separation among the scatterers when they are located on the ϕ direction is needed in order to correctly and reliably extract the features of the scene. On the other hand, if the multiple scatterers are located on a different direction, the algorithm shows very good performance ($P_{c.e.} \geq 80\%$) even for very close scatterers.

However, the combination of multiple images allows enhancement of the spatial resolution of the MSAR image, and in particular to improve the resolution along the major axis of

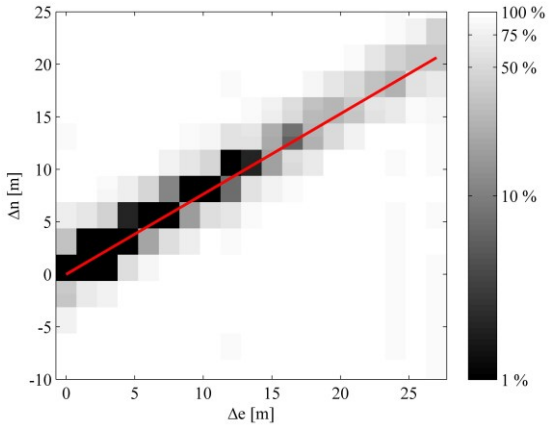

Fig. 5. Probability of correct feature extraction over the $(\Delta\mathrm{e}, \Delta\mathrm{n})$ plane for the bistatic case (Δp = 10 m, ΔA = 0.5).

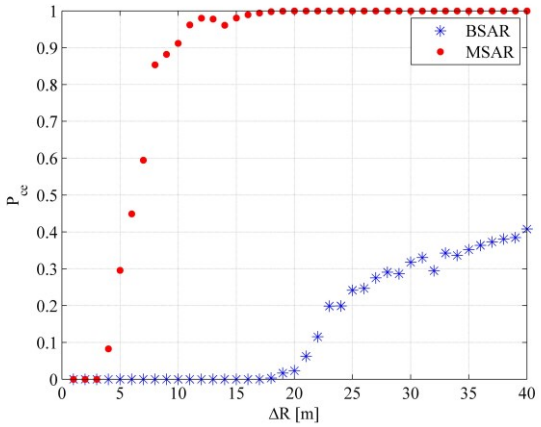

Fig. 6. Probability of correct feature extraction for points over the major axis of the resolution ellipse – comparison bistatic – multistatic performance (Δp = 10 m, ΔA = 0.5).

the single intersecting resolution ellipses. As a consequence, with respect the results in Fig. 5, an improved $P_{c.e.}$ is expected on the direction of the PSF concerning the geometry #1 if a multistatic scenario is considered. To highlight this point we emulate the bistatic image concerning the geometry #2 and then we non-coherently combine them with the respective image concerning geometry #1 to form the multistatic image. The multistatic CLEAN as in Section IIIB is applied and the scattering centers are extracted. It is worth to recall that the multistatic CLEAN allows to estimate for the same scatterer N values of its amplitude, one for each BSAR involved in the system. Therefore, in order to compare the performance with the previous bistatic case, in the multistatic scenario the mean value $0.5(A_{1,k} + A_{2,k})$ is compared with the threshold ΔA. Fig. 6 shows the comparison between the $P_{c.e.}$ obtained in the bistatic (geometry #1) and multistatic cases for the second scatterer located at distance ΔR onto the direction ϕ_1 (i.e. the direction depicted as the red line in Fig. 5); the enhanced capability of the technique to extract the correct positions and amplitudes of the scatterers when it deals with multistatic images is easily recognized.

As a consequence of this enhanced capability of the multistatic CLEAN to correctly sense and extract the point-like

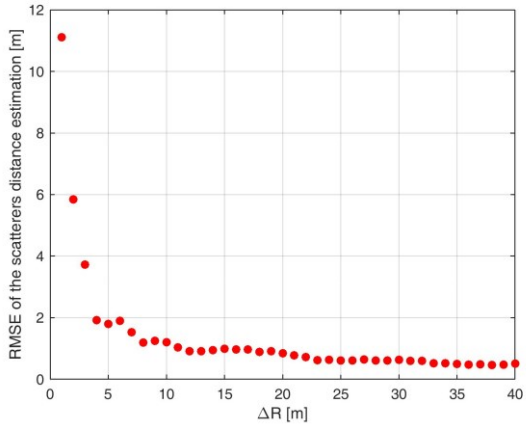

Fig. 7.Root Mean Square Error of the scatterers distance estimation in the multistatic case.

TABLE III
SIMULATED PARAMETERS

k	i	$A_{i,k}$	e_k [m]	n_k [m]
1	1	1	-155	-120
	2	0.5		
2	1	0.5	-150	-130
	2	1		

TABLE IV
BISTATIC AND MULTISTATIC CLEAN RESULTS

k	*image*	$A_{1,k}$	$A_{2,k}$	e_k [m]	n_k [m]
1	BSAR 1	0.92	-	-155.60	-120.68
	BSAR 2	-	0.48	-149.42	-121.15
	MSAR	0.88	0.48	-155.41	-120.07
2	BSAR 1	0.45	-	-150.95	-130.89
	BSAR 2	-	0.90	-144.60	-130.91
	MSAR	0.54	0.92	-150.58	-120.89

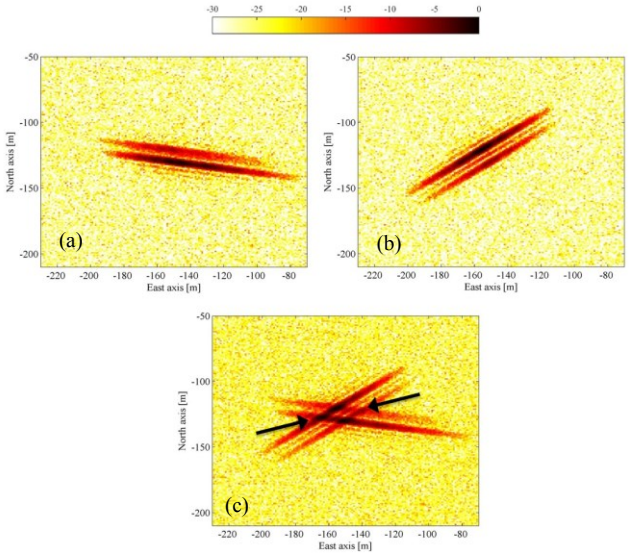

Fig. 8. Emulated GNSS-based SAR images of two point scatterers – a) BSAR image 1,b) BSAR image 2, c) MSAR image.

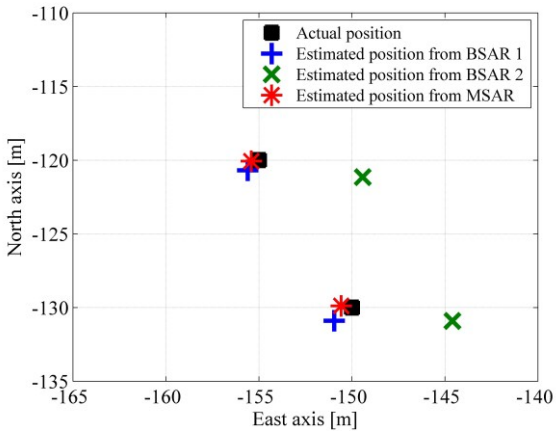

Fig. 9. Comparison actual vs estimated position by the bistatic and joint bi/multi-multistatic CLEAN.

features in the imaged area, a more accurate identification of the structure of the scene may be obtained. To quantify the performance of the proposed technique at sensing features in the scene we specifically refer to the evaluation of the distance between the two extracted scattering centers. Fig. 7 shows the Root Mean Square Error (RMSE) of the estimation of the distance ΔR between the two scatterers aligned onto the direction ϕ_1. We can observe that a high accuracy in estimating such distance is achieved even for very close scatterers, being the RMSE lower than 1m for scatterers at a distance greater than 5-6 m, therefore allowing for a reliable sensing of the surface feature of the observed area.

The previous analysis considered the case of a BSAR image composed by multiple targets lying within the resolution ellipse direction. A different multistatic scenario is given by scattering centers being not aligned in any of the directions of the resolution ellipses. Here, as example, such a scenario is considered by emulating two BSAR images corresponding to the geometry in Table II, composed by two scattering centers whose positions and amplitudes are reported in Table III (in both the images the peak SNR is 25 dB). The two BSAR images and the resulting MSAR image are shown in Fig. 8. The CLEAN algorithms have been applied, and the results are reported in Table IV. Fig. 9 compares the actual and estimated location of the scattering centers from the three images. As it is apparent, the best results in localizing the scattering centers are achieved in the multistatic case, as a direct consequence of the enhanced resolution provided by the multistatic system. We also point out that different amplitudes of the same scattering center in the two BSAR images have been considered. The results reported in Table IV show the effectiveness of the multistatic CLEAN in recovering the variation of the scatterers'

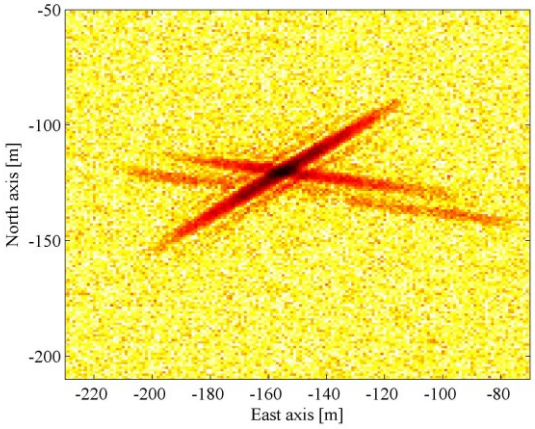

Fig. 10. Residual MSAR image after the first iteration of the joint bi/multi-static CLEAN.

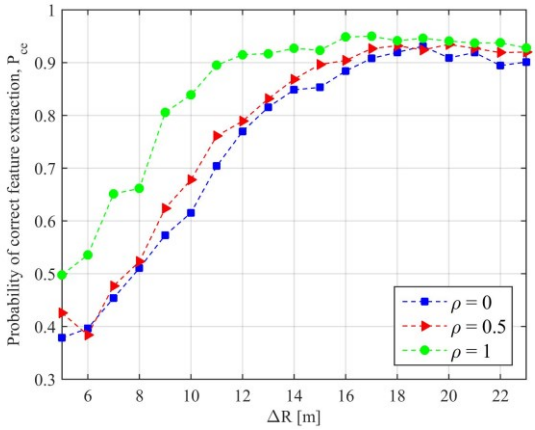

Fig. 11. Probability of correct feature extraction in presence of ghost scatterers.

amplitude in different images.

As previously stated, one of the issue arising in multistatic radar is the presence of ghost targets. In the MSAR image in Fig. 8c four high intensity returns can be recognized, appearing as a consequence of the summation of the single bistatic images: two of them are due to the intersection of the PSFs from the same point targets, and therefore they represent the multistatic return from real scattering centers, whereas the other two (pointed by the arrows in the figure) are due to the intersections of the PSFs concerning different scattering centers; the latter are artefacts arising from the MSAR formation process. Therefore, on one hand the MSAR image can isolate a greater number of scatterers with respect to the bistatic case due to the resolution improvement, but on the other hand it has to handle the presence of artefacts. However, observing the position of the estimated scatterers in Fig. 9 we can notice that the multistatic CLEAN does not recognize the bright spots concerning the artefacts as real scattering centers locations, therefore acting like a deghosting technique. The ghost-rejection ability of the technique is due to the iterative procedure of cancellation of the detected scatterers from the residual image. In order to illustrate such a concept, Fig. 10 shows the residual multistatic image after the extraction and cancellation of the first main scatterer: the strongest peak of the MSAR, which corresponds to a real multistatic scattering center, is selected and the corresponding response $\hat{\mathrm{S}}_1$ is estimated; then, I_{test} is updated, resulting in the residual image shown in Fig. 10; we can observe that by cancelling $\hat{\mathrm{S}}_1$ from the image under test, the intersections of the PSFs originating the ghosts disappear.

It should be clarified that the presented method cannot have the unrealistic objective of a perfect unambiguous extraction of the actual scatterers positions. A quantitative analysis of the deghosting performance is here provided as follows. A multistatic image composed by two scatterers is emulated by employing the experimental PSFs in Table II, and by placing the two scatterers in $\boldsymbol{P}_1$ and $\boldsymbol{P}_2$ such that they are aligned onto the direction $\phi_M = \frac{\phi_1+\phi_2}{2}$ at distance $\Delta R = |\boldsymbol{P}_1 - \boldsymbol{P}_2|$. In such conditions, it is easy to verify that the bistatic responses intersect in four distinct points, two actual and two false scatterer positions, respectively, provided that the value of ΔR is such that the following conditions are satisfied: 1) in each bistatic image the two mainlobes corresponding to the two scatterers are not superimposed; 2) the mainlobe of a given scatterer in the first bistatic image intersects the mainlobe of the other scatterer in the second bistatic image. The complex amplitudes of the scatterers in each BSAR image are considered as independent random variables following complex Gaussian distributions, with mean intensity I_1 and $I_2 = \gamma I_1$, respectively. A correlation coefficient ρ is assumed between the complex amplitudes of each scatterer in the two BSAR images. The two imaged scatterers are assumed embedded in a Gaussian background with proper signal to noise power ratio, SNR. For each ΔR under test, 1000 independent trials have been performed. For each trial, the extracted scatterers have been associated with one of the set $\{\boldsymbol{P}_1, \boldsymbol{P}_2, \boldsymbol{G}_a, \boldsymbol{G}_b\}$ on the basis of a nearest neighbor criteria, where $\boldsymbol{G}_a$ and $\boldsymbol{G}_b$ are the positions of the ghosts; let r_{ik} be the line through the kth scatterer on the direction ϕ_i, then ghosts positions can be defined as $\boldsymbol{G}_a = \{r_{12} \cap r_{21}\}$ and $\boldsymbol{G}_b = \{r_{11} \cap r_{22}\}$. A correct feature extraction is assumed if the extracted scatterers are associated with $\boldsymbol{P}_1$ and $\boldsymbol{P}_2$, and no scatterer is associated with a ghost. Fig. 11 shows the obtained probability of correct feature extraction for different ρ values having set SNR to 25 dB and $\gamma = 1$. As we can observe, when the correlation between the two images increases, better performance is achieved. This behavior can be easily explained considering that the main reason for which the technique can recognize the bright spot locating in $\boldsymbol{G}_a$ or $\boldsymbol{G}_b$ as a scatterer is that it corresponds to the point of highest intensity in the MSAR image. When the amplitude of the scatterers shows a considerable fluctuation as imaged in the two BSAR images, such a situation may occur. In this regard, it is also worth to notice that the condition $\gamma = 1$ represents the worst case. Indeed, if one of the scatterers is dominant with respect the other one (i.e. $\gamma < 1$), it will have a higher probability to be extracted first, thus deleting the intersections originating the

ghosts. Nevertheless, despite the challenging conditions, a high probability to correctly recovering the actual scatterers avoiding to extract the ambiguities has been obtained, higher than 90% for scatterers at a distance greater than about 15 m.

The above analysis proves the effectiveness of the algorithm in providing a low rate of extraction of false scatterers, allowing the proper identification of the main scatterers even in condition of close scattering centers. Obviously, some losses are expected in complex scenarios where a great number of scatterers can be involved.

V. Feature Extraction from Real GNSS-based SAR Images

An acquisition campaign, Fig. 12, was conducted in order to obtain a set of real GNSS-based SAR images. The experimental hardware (Fig. 12a) comprises a super-heterodyne receiver developed at the University of Birmingham (UK). The receiver has two channels: one uses a low gain antenna to collect the direct signal from the satellite which is used for the synchronization, providing the propagation delay and phase reference for the image formation (heterodyne channel HC); the other is the radar channel (RC), using a high-gain antenna pointed toward the target area and collecting the reflected signal. The receiver was located onto the roof of the School of Electronic, Electrical and Computer Engineering of the University of Birmingham, and the RC antenna was pointed toward Metchley Park, located toward West, see Fig. 12b. Experiments were conducted using three GLONASS satellites as transmitters, whose positions are sketched in Fig. 12c; the angular positions of the satellites with respect to the receiver location are reported in Table V (azimuth angles measured clockwise starting from the East direction).

On the image formation level, BSAR images were computed via a back-projection [11] on the same reference grid on the ground, with the location of the reference (HC) antenna, whose position was measured via a professional GPS receiver with Real Time Kinematic (~1cm positioning accuracy), as the origin of the ENU reference system. Then, a final correction stage is based on artificially shifting the brightest compressed echo in the image on the origin, since it corresponds to the direct signal recorded through the antenna sidelobes before overlaying the image to a Google Earth photograph of the scene. Of course there may be residual errors with this approach, however a comparison between the individual images and the photographs shows objects, such as tree lines and sparse buildings, as well as grassy areas, which are registered in the correct region and therefore we do not consider geocoding as a major source of error in our evaluation. The resulting BSAR images are shown in Fig. 13, superimposed to the optical photo of the area. It is possible to observe that since the satellites are in different positions, bistatic images of the same scene are different. Different objects could be highlighted, and, as it is evident looking at the images, the PSFs have different orientations. The CLEAN techniques were then applied in order to extract the useful information.

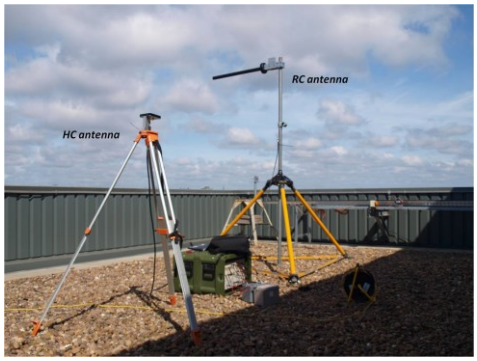

(a)

(b)

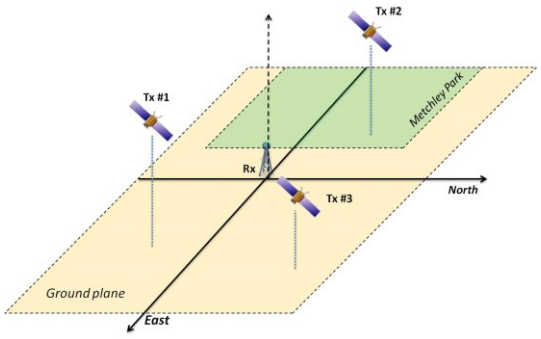

(c)

Fig. 12. Acquisition campaign – experimental hardware (a), target area (b) and satellite positions (c).

TABLE V
ACQUISITION PARAMETERS

#	Azimuth angle [deg]	Elevation angle [deg]
1	8	53
2	220	71
3	-15	75

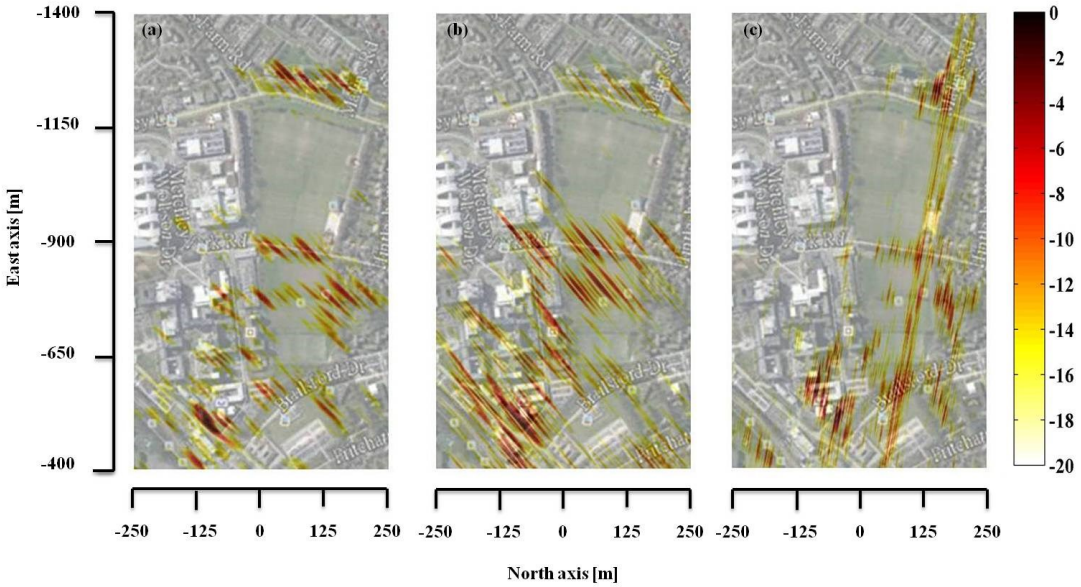

Fig. 13. Experimental images - BSAR #1 (a), BSAR #2 (b) and BSAR #3 (c).

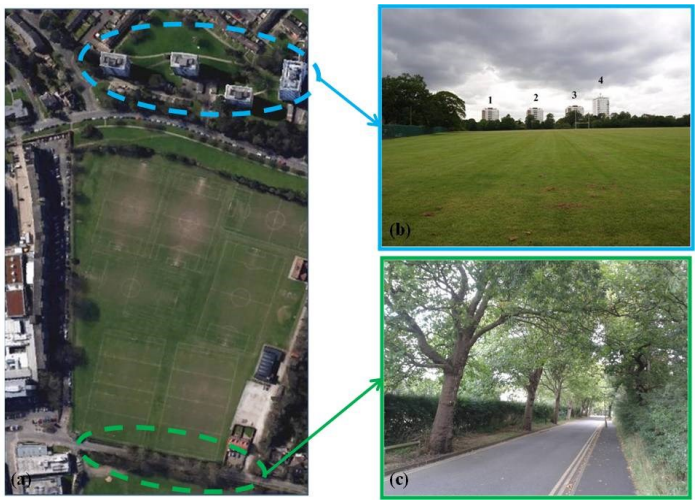

Fig. 14. Metchley Park area – sport pitches (a), buildings at far end (b) and tree lines at middle range (c).

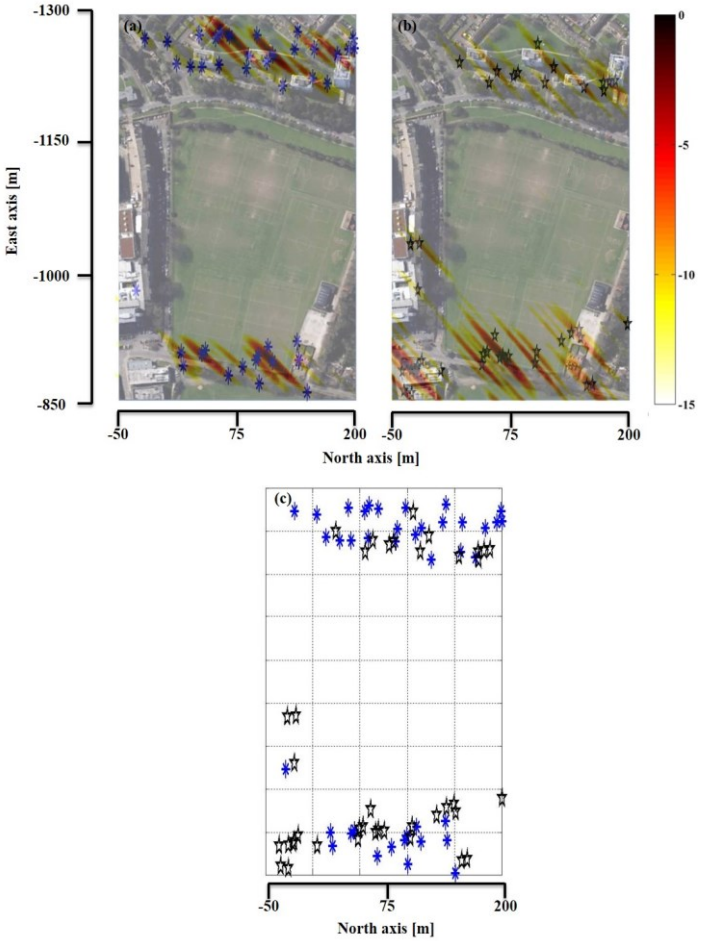

Fig. 15. Multi-perspective analysis – BSAR #1 (a), BSAR #2 (b) and scatterers map (c).

A. Multi-perspective analysis

As we can observe from Fig. 12c, satellites #1 and #2 illuminate the target area from very different view angles. In such a case, we can foresee that different objects have been highlighted in the resulting SAR images. Therefore, in this case it is of interest to extract the information separately from each image and then to combine them (multi-perspective analysis). For this purpose, the coherent bistatic CLEAN described in Section IIIA was applied separately against BSAR images #1 and #2, with a focus on the grassy area highlighted in Fig. 14a (Metchley Park sport pitches), bounded by a group of buildings at approximately 1300 meters range (Fig. 14b) and tree lines at approximately 880 meter range (Fig. 14c).

Fig. 15a and b show the BSAR images concerning the selected area, superimposed to the optical photo, for images #1 and #2, respectively. The blue '*' and the black '☆' markers indicate the estimated position of the detected scatterers in the scene. In both the images, clusters of scatterers have been found in patches of the images corresponding to the regions occupied

by the tree lines and the buildings; also, none scatterer has been revealed in the region corresponding to the grass. Therefore, the application of the CLEAN technique to the bistatic images allows to extract the macro-feature of the scene, whose structure can be identified with an enhanced degree of accuracy by combining the single images information, for example forming a scatterers map as shown in Fig. 15c.

B. *Multistatic image analysis*

BSAR images #1 and #3 have been acquired from closer view angles with respect to the previous case. Also, as we can observe looking at the orientation of the bright spots composing the two images, different PSF orientations have been achieved. Therefore, the corresponding MSAR image, obtained by a non-coherent summation of BSAR images #1 and #3 (Fig. 16), is characterized by an enhanced spatial resolution, thus making possible a more precise identification of the features of the scene.

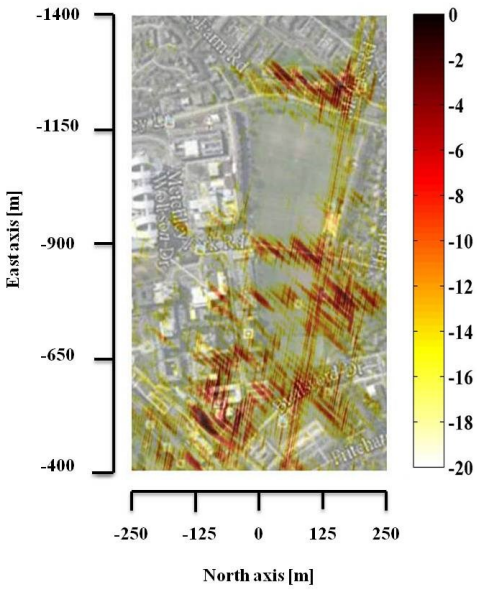

Fig. 16. Experimental MSAR image.

As a case study, we analyze the area corresponding to the tree lines. The reason of this choice is that for L-band transmissions and with long integration times, the main contributor to their reflectivity is their trunk, which is roughly of cylindrical shape. As a consequence, an acceptable degree of correlation is expected among the considered images in terms of scattering centers position. Fig. 17 shows the bistatic and the corresponding multistatic images concerning the selected area, superimposed on an optical photograph, where the markers indicate the position of the scatterers identified by applying the CLEAN techniques. Fig. 18 shows the comparison between the scattering positions extracted and the real location of individual trees.

In Fig. 17a,b we can observe that the bistatic CLEAN technique recognized the presence of a number of scatterers (Fig. 17a,b), but the coarse resolution severely affects the accuracy of their localization and as a consequence a large leakage of the detected scatterers around the true locations of the tree lines can be observed (Fig. 18a,b). It is interesting to observe that in both the BSAR images the PSFs are oriented so that the returns of trees located on the left and right side of the road give rise to single elliptical spots; as analyzed in Fig. 5-Fig. 6, in the case of multiple scatterers located onto the direction of the orientation of the PSF, the bistatic CLEAN shows poor performance in recognizing single scattering

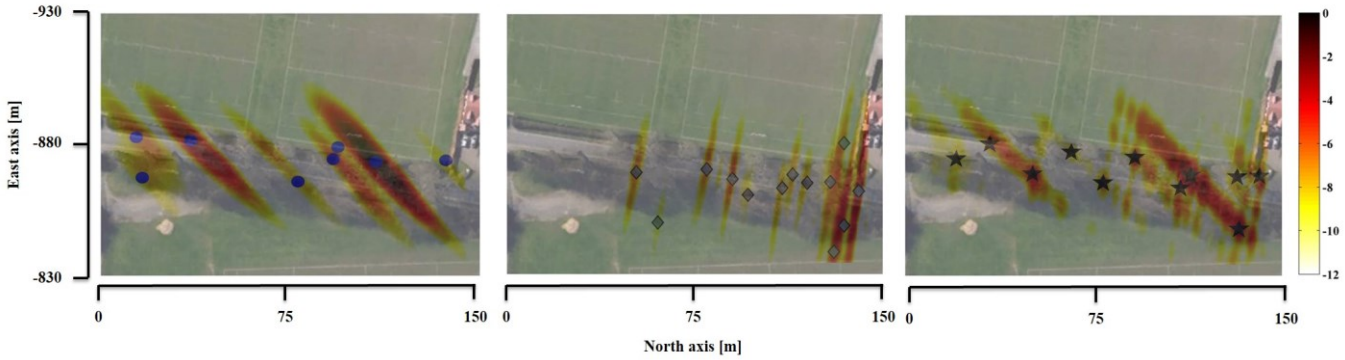

Fig. 17. Tree lines at the middle range – BSAR #1 (a), BSAR #2 (b) and MSAR (c).

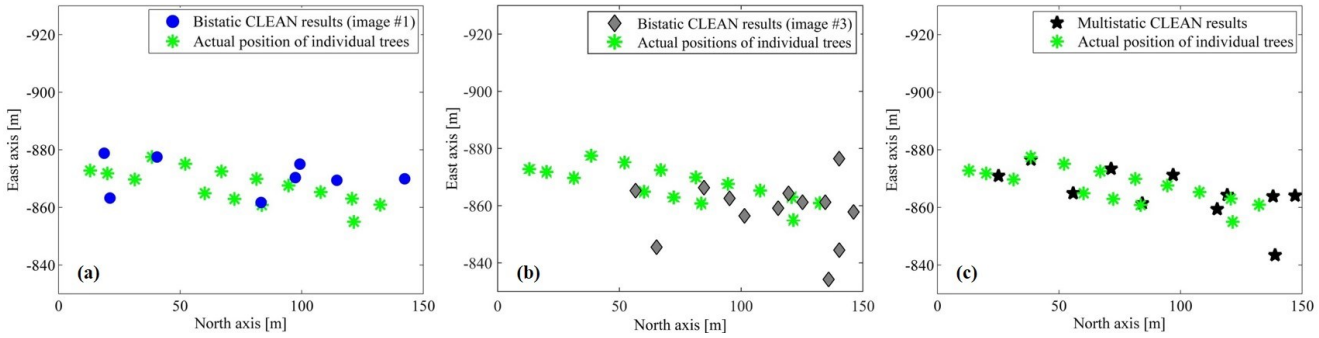

Fig. 18. Comparison actual position of individual trees and dominant scatterers extracted by the CLEAN algorithms - BSAR #1 (a), BSAR #2 (b) and MSAR (c).

TABLE VI
FEATURE EXTRACTION PERFORMANCE FOR THE TREE-LINES AREA

# Tree[*]	*δp BSAR #1* [m]	*δp BSAR #3* [m]	*δp MSAR* [m]
1	2.10	-	1.01
2	-	-	-
3	-	-	4.56
4	-	4.90	-
5	3.93	5.04	4.32
6	-	-	-
7	8.91	2.14	1.91
8	-	2.20	6.48
9	-	-	-
10	7.11	-	5.22
11	-	-	-
12	-	3.52	4.29
13	-	-	-
14	0.95	-	0.90
15	-	7.27	7.69
Mean error	4.60	4.18	4.04
Sensed trees	5/15	6/15	9/15

[*] top tree line: trees 1-8 (from left to right); bottom tree line: trees 9-15 (from left to right).

centers correctly.

Fig. 17c shows the case concerning the multistatic image, and the black star markers localize the extracted position of the scattering centers by applying the multistatic CLEAN: we can observe that in this case both the tree lines running along the road have been identified. Looking at the comparison between the scattering positions extracted by the multistatic CLEAN and the real location of individual trees in Fig. 18c, we can appreciate a considerably greater matching between the CLEAN results and the ground truth than the bistatic cases even if not all the real tree locations have been detected, as a consequence of their close positions. In order to determine quantitatively the obtained sensing performance, the trees and the estimated scatterers have been associated by means of a nearest neighbour criterion. A tree is considered sensed if a scatterer still not associated with another tree has been detected at a maximum distance of 10 m. For both the considered bistatic images and for the corresponding multistatic one Table VI reports the errors in tree locations δp for the 15 actual trees; the last two rows of the table report the mean error in tree location and the number of effectively sensed trees. From the table, it is possible to observe that not all the trees have been sensed by the algorithm, both for the bistatic and multistatic images. Nevertheless, comparing the results achieved for the bistatic and multistatic cases, it is possible to observe that enhanced performance have been obtained exploiting the multistatic data: indeed, as well as a slight improvement in recovering the individual tree positions, a greater number of trees has been sensed moving from 5 (BSAR #1) and 6 (BSAR #2) sensed trees out of 15 to 9 in the multistatic image. Therefore, in the multistatic scenario we have the potential not only in discriminating macro-features of the scene, but even punctual features, so that a more accurate description of the scene structure can be obtained, as a direct consequence of the enhanced spatial resolution. It is also worth to note that not all the bright spots appearing in the multistatic image correspond to the location of the trees, for example the cluster of bright returns around (80 m, -900 m) in Fig. 17c. As previously discussed, they can be considered as artefacts arising from the MSAR image formation process. However, the multistatic CLEAN successfully does not consider the major part of such ambiguities as actual scatterers. For example, none of the ambiguities around (80 m, -900 m) has been sensed as an actual tree location, and only an individual spot of the similar cluster around (130 m, -840 m) has been confused with a tree. Therefore, this method considerably alleviates the ambiguities problem, reducing the number of detected ghosts. Such results achieved against experimental data are in good agreement with the previously shown theoretical performance analysis thus supporting the practical applicability of the proposed technique.

VI. CONCLUSION

This paper addresses a passive multistatic SAR system based on GNSS transmission. A single receiver located near the ground can collect the signals coming from multiple satellites, and therefore a set of different bistatic images of the same area can be obtained. The exploitation of different, spatially separated satellites allows to perform a multi-perspective analysis of the area, consisting in extracting the main features of the scene from each individual image and subsequently combine the information, thus enhancing the image information space. Also, the single images can be combined at the image level to form a multistatic image, and the features can be subsequently identified. To these purposes, ad-hoc CLEAN algorithms have been developed able to deal with GNSS-based SAR images and allowing the extraction of the dominant scattering centers of the images.

In the case of widely separated satellites, variation of the position of the dominant scattering canters is expected; by means of a bistatic CLEAN, the scattering centers are extracted from the individual images and then the information are merged to form a scatterer's map. Simulated and experimental results showed the effectiveness of this approach to identify the macro structure of the area.

In the case of a limited variation of the satellite perspective, a multistatic image can be obtained characterized by dominant scattering centers having very similar location in the single bistatic images. In such a case the point-features can be detected directly from the multistatic image. Since images obtained from differently located satellites have differently oriented image responses, the GNSS-based MSAR image may be characterized by a drastically improved PSF with respect to the BSAR images. As a consequence, better performance than the bistatic

case can be reached and more information can be extracted from the scene. In the case of close scattering centers, enhanced feature extraction performance are obtained and the ghost targets arising from the multistatic image formation process may be rejected. Both these qualities of the multistatic approach have been proved again simulated and experimental images, showing the effectiveness of the multistatic approach to extract not only macro-feature of the scene, but even details.

It is worth to mention that all the results hold also for the configuration involving a moving receiver, where a Doppler resolution less than 1 m can be obtain; consequently, a further enhanced capability of the proposed techniques to extract information from the observed area is expected.

Finally, it is important to state that the developed techniques are not specific to passive GNSS-based systems, but can be used in principle on all multi-static SAR systems, especially those possessing a coarse range resolution.

REFERENCES

[1] S. Jin, G.P. Feng, S. Gleason, "Remote sensing using GNSS signals: Current status and future directions," *Adv. Space Res.*, vol. 47, Issue 10, pp. 1645-1653, May 2011.

[2] M. Martin-Neira, S. D'Addio, C. Buck, N. Floury, R. Prieto-Cerdeira, "The PARIS Ocean Altimeter In-Orbit Demonstrator," *IEEE Trans on Geosci. and Remote Sens.,* vol. 49, no. 6, pp. 2209-2237, June 2011.

[3] K. Yu, C. Rizos, A. Dempster, "GNSS-Based Model-Free Sea Surface Height Estimation in Unknown Sea State Scenarios," *IEEE J. Sel. Topics Appl. Earth Observ. Remote Sens.*, vol. 7, no. 5, pp. 1424-1435, May 2014.

[4] E. Valencia, A. Camps, N. Rodriguez-Alvarez, H. Park, I. Ramos-Perez, "Using GNSS-R Imaging of the Ocean Surface for Oil Slick Detection," *IEEE J. Sel. Topics Appl. Earth Observ. Remote Sens.*, vol. 6, no. 1, pp. 217-223, Feb. 2013.

[5] A. Egido, S. Paloscia, E. Motte, L. Guerriero, N. Pierdicca, M. Caparrini, E. Santi, G. Fontanelli, N. Floury, "Airborne GNSS-R Polarimetric Measurements for Soil Moisture and Above-Ground Biomass Estimation," *IEEE J. Sel. Topics Appl. Earth Observ. Remote Sens.*, vol. 7, no. 5, pp.1522-1532, May 2014.

[6] A. Komjathy, M. Armatys, D. Masters, P. Axelrad, V. Zavorotny, and S. Katzberg, "Retrieval of Ocean Surface Wind Speed and Wind Direction Using Reflected GPS Signals," *J. Atmos. Oceanic Technol.*, 21, 515–526, 2004.

[7] V. Koch, R. Westphal, "New approach to a multistatic passive radar sensor for air/space defense," *IEEE Aerosp. Electron. Syst. Mag.*, vol. 10, no. 11, pp. 24-32, Nov. 1995.

[8] A. Dempster, E. P. Glennon, C. Rizos, "Feasibility of air target detection using GPS as a bistatic radar," *J. Global Positioning Syst.*, vol. 5, no. 1-2, pp. 119-126, 2006.

[9] C. Clemente, J.J. Soroghan, "GNSS-based passive bistatic radar for micro-Doppler Analysis of Helicopter Rotor Blades," *IEEE Trans. Aerosp. Electron. Syst.*, vol. 50, no. 1, pp. 491-500, Jan. 2014.

[10] M. Cherniakov and T. Zeng, "Passive bistatic SAR with GNSS transmitters," in *Bistatic Radar: Emerging Technology*, M. Cherniakov, Ed. New York, NY, USA: Wiley, 2008.

[11] M. Antoniou, M. Cherniakov, "GNSS-based SAR: A signal processing view," *EURASIP J. Adv. Signal Process.*, 2013:98, May 2013.

[12] X. He, M. Cherniakov, T. Zeng, "Signal detectability in SS-BSAR with GNSS non-cooperative transmitter," *IET Proc. Radar Sonar Navig.*, vol. 152, no. 3, pp. 124-132, June 2005.

[13] M. Antoniou, Z. Zeng, L. Feifeng, M. Cherniakov, "Experimental demonstration of passive BSAR imaging using navigation satellites and a fixed receiver," *IEEE Geosci. Remote Sens. Lett.*, vol. 9, no. 3, pp. 477-481, May 2012.

[14] F. Liu, M. Antoniou, Z. Zeng, M. Cherniakov, "Coherent Change Detection using Passive GNSS-based SAR: experimental proof of concept," *IEEE Trans. Geosci. Remote Sens.*, vol.51, no.8, pp.4544-4555, August 2013.

[15] Q. Zhang, M. Antoniou, W. Chang, M. Cherniakov, "Spatial Decorrelation in GNSS-Based SAR Coherent Change Detection," *IEEE Trans. Geosci. Remote Sens.*, vol. 53, no. 1, pp. 219-228, Jan. 2015.

[16] M. Antoniou, H. Zhou, Z. Zeng, R. Zuo, Q. Zhang, M. Cherniakov, "Passive BSAR imaging with Galileo transmitters and a moving receiver: experimental demonstration," *IET Proc. Radar, Sonar Navig.*, vol. 7, no. 9, pp 985-993, 2013.

[17] T. Zeng, T. Zhang, W. Tian, and C. Hu, "A novel subsidence monitoring technique based on space-surface bistatic differential interferometry using GNSS as transmitters," *Sci China Inf Sci*, 2015, 58.

[18] F. Liu, M. Antoniou, Z. Zeng, M. Cherniakov, "Point Spread Function analysis for GNSS-based SAR with long dwell times - theory and experimental confirmation," *IEEE Geosci. Remote Sens. Lett.*, vol. 10, no. 4, pp. 781-785, Jul. 2013.

[19] H. Ma, M. Antoniou, and M. Cherniakov, "Passive GNSS-based SAR resolution improvement using joint Galileo E5 signals," *IEEE Geosci. Remote Sens. Lett*, vol. 12, no. 8, pp. 1640-1644, Aug. 2015.

[20] F. Santi, M. Antoniou, and D. Pastina, "Point Spread Function Analysis of GNSS-Based Multistatic SAR," *IEEE Geosci. Remote Sens. Lett*, vol. 12, no. 2, pp. 190-194, Feb. 2015.

[21] F. Santi, D. Pastina, M. Bucciarelli, M. Antoniou, D. Tzagkas, M. Cherniakov, "Passive multistatic SAR with GNSS transmitters: preliminary experimental study," in *Proc. 11th EuRAD Conf.*, Rome, Italy, Oct. 2014, pp. 129-132.

[22] M. Vespe, C.J. Baker and H.D. Griffiths, "Radar target classification using multiple perspectives," *IET Radar, Sonar Navig.*, vol. 1, no. 4, pp. 300-307, Aug. 2007.

[23] Z. Zeng, M. Antoniou, Q. Zhang, M. Hui, M. Cherniakov, "Multi-perspective GNSS-based passive BSAR: preliminary experimental results," in *Proc. 14th Int. Radar Symp.*, Jun. 2013, pp. 467-472.

[24] T. Zeng, D. Ao, C. Hu, T. Zhang, F. Liu, W. Tian, K. Lin, "Multianlge BSAR imaging based on BeiDou-2 navigation satellite system: experiments and preliminary results," *IEEE Trans. Geosci. Remote Sens.*, vol. 53, no. 10, pp. 5760-5773, Oct. 2015.

[25] Z. Jianxiong, S. Zhiguang, C. Xiao, F. Qiang, "Automatic Target Classification of SAR Images Using Global Scattering Center Model," *IEEE Trans. Geosci. Remote Sens.*, vol. 49, no. 10, pp. 3713-3729, Oct. 2011.

[26] F. Tupin, H. Maître,J.-F. Mangin, J.-M. Nicolas, E. Pechersky, "Detection of linear features in SAR images: application to road network extraction," *IEEE Trans. Geosci. Remote Sens.*, vol. 36, no. 2, pp. 434-453, March 1998.

[27] C. D'Elia, S. Ruscino, M. Abbate, B. Aiazzi, S. Baronti, L. Alparone, "SAR Image Classification Through Information-Theoretic Textural Features, MRF Segmentation, and Object-Oriented Learning Vector Quantization," *IEEE J. Sel. Topics Appl. Earth Observ. Remote Sens*, vol. 7, no. 4, pp. 1116-1126, Apr. 2014.

[28] J. Tsao and B. D. Steinberg, "Reduction of sidelobe and speckle artifacts: The CLEAN technique," *IEEE Trans. Antennas Propag.*, vol. 36, no. 4, pp. 543-556, Apr. 1988.

[29] S. Choi and H. T. Kim, "Two-dimensional evolutionary programming-based CLEAN," *IEEE Trans. Aerosp. Electron. Syst.*, vol. 39, no. 1, pp. 373-382, Jan. 2003.

[30] H. Ghaemi, M. Galletti, T. Boerner, F. Gekat, M. Viberg, "CLEAN technique in strip-map SAR for high-quality imaging," in *Proc. 2009 IEEE Aereospace Conf.*, March 2009, pp. 1-7.

[31] F. Santi, M. Bucciarelli, D. Pastina, M. Antoniou, "CLEAN technique for passive bistatic and multistatic SAR with GNSS transmitters," in *2015 IEEE Radar Conference (RadarCon)*, Arlington, VA, 2015, pp. 1228-1233.

[32] M. Antoniou, M. Cherniakov, C. Hu, "Space-Surface Bistatic SAR Image Formation Algorithms," *IEEE Trans. Geosci. Remote Sens.*, vol. 47, no. 6, June 2009, pp. 1827-1843.

[33] T. Zeng, M. Cherniakov, and T. Long, "Generalized Approach to resolution analysis in BSAR," *IEEE Trans. Aerosp. Electron. Syst.*, vol. 41, no. 2, pp.461-471, Apr. 2005.

[34] A. Moccia, "Fundamentals of Bistatic Synthetic Aperture Radar," in *Bistatic Radar: Emerging Technology*, M. Cherniakov, Ed. New York, NY, USA: Wiley, 2008.

[35] N. J. Willis and H. Griffiths (Eds.), *Advances in Bistatic Radar*, Raleigh NC, USA: SciTech Publishing, 2007.